Atomic Structure and Electrical Activity of Grain Boundaries and Ruddlesden–Popper Faults in Cesium Lead Bromide Perovskite

Arashdeep Singh Thind, Guangfu Luo, Jordan A. Hachtel, Maria V. Morrell, Sung Beom Cho, Albina Y. Borisevich, Juan-Carlos Idrobo, Yangchuan Xing, and Rohan Mishra*

To evaluate the role of planar defects in lead-halide perovskites—cheap, versatile semiconducting materials—it is critical to examine their structure, including defects, at the atomic scale and develop a detailed understanding of their impact on electronic properties. In this study, postsynthesis nanocrystal fusion, aberration-corrected scanning transmission electron microscopy, and first-principles calculations are combined to study the nature of different planar defects formed in $CsPbBr_3$ nanocrystals. Two types of prevalent planar defects from atomic resolution imaging are observed: previously unreported Br-rich $[001](210)\sum 5$ grain boundaries (GBs) and Ruddlesden–Popper (RP) planar faults. The first-principles calculations reveal that neither of these planar faults induce deep defect levels, but their Br-deficient counterparts do. It is found that the $\sum 5$ GB repels electrons and attracts holes, similar to an n–p–n junction, and the RP planar defects repel both electrons and holes, similar to a semiconductor–insulator–semiconductor junction. Finally, the potential applications of these findings and their implications to understand the planar defects in organic–inorganic lead-halide perovskites that have led to solar cells with extremely high photoconversion efficiencies are discussed.

Lead-halide perovskites, such as $CH_3NH_3PbI_3$ and $CsPbBr_3$, have recently emerged as a promising family of low-cost, high-performance semiconductors for a variety of applications including in solar cells, solid-state lighting, lasing, and photocatalysis.[1] The bandgap of these perovskites can be tuned over a wide range for targeted applications by changing the cation or anion composition. Furthermore, they can be fabricated on a large scale over different substrates using low-cost solution-based methods.[2,3] In traditional semiconductors, defects often deleteriously affect the performance and require the use of expensive accurately controlled growth techniques to minimize the formation of defects. Conversely, in lead-halide perovskites, most point defects with low formation energies, such as vacancies, only give rise to shallow defect levels. Point defects, such as cation antisites and Pb interstitials, that lead to deep defect levels and nonradiative recombination centers have high formation energies and are only present in low concentrations.[4,5] Therefore, the electronic properties of lead-halide perovskites are found to be comparatively resistant to a large concentration of point defects that generally accompany solution-based growth techniques used to grow them.[4–6] Nonetheless, their performance can still be substantially improved by careful control over these deep-level point defects. For instance, an extremely high-power conversion efficiency of 19.1% in large-area solar cells was recently demonstrated by growing formamidinium-lead-halide-based perovskites under iodine-rich conditions that minimized the concentration of the deep-level defects.[7]

Besides point defects, the solution-based growth also leads to polycrystalline materials with abundant grain boundaries (GBs) and other planar faults.[8,9] There have been diverging experimental reports on the electrical activity of GBs in lead-halide perovskites. While some groups reported GBs to be electrically benign,[10] or even beneficial for charge transport,[11] others have shown that GBs act as nonradiative recombination centers and their passivation leads to improved carrier separation.[12–14] Atomic-scale modeling of hypothetical GBs—derived from analog of GBs in inorganic oxide perovskites, such as $SrTiO_3$,

A. S. Thind, Prof. R. Mishra
Institute of Materials Science & Engineering
Washington University in St. Louis
St. Louis, MO 63130, USA
E-mail: rmishra@wustl.edu
Dr. G. Luo, Dr. S. B. Cho, Prof. R. Mishra
Department of Mechanical Engineering & Materials Science
Washington University in St. Louis
St. Louis, MO 63130, USA
Dr. J. A. Hachtel, Dr. J.-C. Idrobo
Center for Nanophase Materials Sciences
Oak Ridge National Laboratory
Oak Ridge, TN 37831, USA
M. V. Morrell, Prof. Y. Xing
Department of Chemical Engineering
University of Missouri
Columbia, MO 65211, USA
Dr. A. Y. Borisevich
Material Science and Technology Division
Oak Ridge National Laboratory
Oak Ridge, TN 37831, USA

ADVANCED
SCIENCE NEWS
www.advancedsciencenews.com
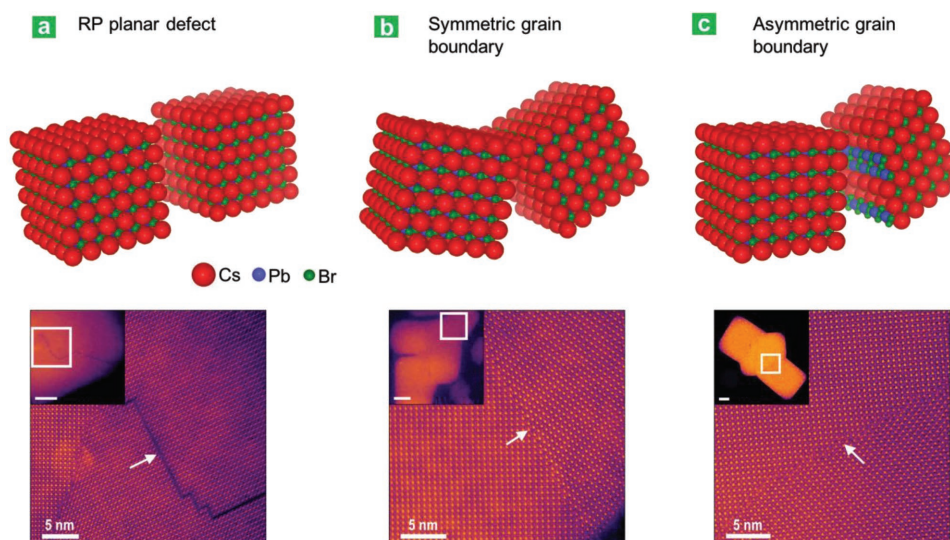
ADVANCED
MATERIALS
www.advmat.de

Figure 1. Schematic of formation of different planar faults during the fusion of CsPbBr$_3$ nanocrystals, and their respective HAADF images: a) RP planar fault, b) symmetric GB, and c) asymmetric GB. Each type of planar defect in these HAADF images is indicated with a white arrow. The insets show low-magnification images of the fused nanocrystals. The scale bars in the insets correspond to 15 nm.

that have been characterized using scanning transmission electron microscopy (STEM)[15]—consistently predict them to be benign without inducing any deep-level defect states.[4,16] However, because these lead-halide perovskites have a significantly larger lattice (>1.5 times) and different electronic structure relative to typical inorganic oxide perovskites, the similarity of their GBs remains an open question. Therefore, to understand the electrical and optical properties of GBs in lead-halide perovskites, there is a need for their atomic-scale imaging.

In this study, we have combined nanocrystal synthesis, STEM characterization, and first-principles modeling to investigate the planar defects in lead-halide perovskite nanocrystals. Given the sensitivity of organic–inorganic lead-halide perovskites to the electron beam in a TEM, we have investigated an inorganic perovskite CsPbBr$_3$, which is significantly more stable than the organic–inorganic lead-halide perovskites.[17] We have used a synthesis process that induces fusion of small nanocrystals to form planar defects.[18] Using STEM Z-contrast imaging, we find the presence of two dominant planar defects: high-angle GBs, such as a previously unreported Br-rich [001](210)∑5 GB, and Ruddlesden–Popper (RP) planar faults. We have combined the atomic structure of these planar defects with density-functional theory (DFT) calculations to obtain their electronic properties. We reveal that the experimentally observed Br-rich GBs and RP planar faults do not induce deep defect levels, but their Br-deficient counterparts do. We predict that the dominant ∑5 GB repels electrons but attract holes, while the RP planar fault repels both electrons and holes. Therefore, both the planar faults are expected to affect charge transport and electron hole recombination in CsPbBr$_3$. Finally, we extend our results to GBs in organic–inorganic lead-halide perovskites to resolve the conflicting experimental reports on their activity.

To carry out postsynthesis fusion of small nanocrystals to allow the formation of planar faults, we have used diethylzinc to remove the surface ligands on colloidally grown CsPbBr$_3$ nanocrystals. Within 48 h, the nanocrystals grow from 8 to

59 nm in lateral dimensions. Further experimental details are provided in the Experimental Section. Depending on the relative position and surface termination of the nanoparticles, we find that the fusion of two nanoparticles can result in three types of planar defects: RP planar fault, symmetric GB, and asymmetric GB, as schematically shown in **Figure 1**a–c, respectively, together with the corresponding high-angle annular dark field (HAADF) images. In HAADF imaging, the contrast is approximately proportional to the square of the atomic number (Z),[19] allowing the atomic species to be identified by their Z-contrast as described later.

Previous studies[20] have shown that the surfaces of CsPbBr$_3$ nanocrystals are terminated with CsBr-rich planes under typical growth conditions. Therefore, it is expected that when two parallel nanocrystals with CsBr-rich (001) surfaces merge, an RP planar fault would be formed (Figure 1a). If the contact surfaces of two nanocrystals are not parallel but have the same surface termination (Figure 1b), a symmetric GB could be formed after significant atomic rearrangement. If the two nanocrystal surfaces have different terminations, an asymmetric GB would be formed (Figure 1c). The overall morphology of CsPbBr$_3$ nanocrystals before and after the fusion can be found in Section S1 in the Supporting Information.

Figure 2a,b shows atomic-resolution HAADF images of a prevalent symmetric GB formed during the fusion process. HAADF images of other less common GBs can be found in Section S2 in the Supporting Information. In Figure 2c, the atomic columns in Figure 2b are labeled according to the histogram of the Z-contrast (Z = 82 for Pb, Z = 55 for Cs, and Z = 35 for Br), as shown in the inset of Figure 2c. The atom-labeled image indicates that the out-of-plane orientation of this GB is CsPbBr$_3$ [001].

To verify our observations, we examine the GB structure from Figure 2b,c using DFT calculations. The DFT-optimized structure shown in Figure 2d is in good agreement with the HAADF image. For instance, in the DFT-optimized structure,
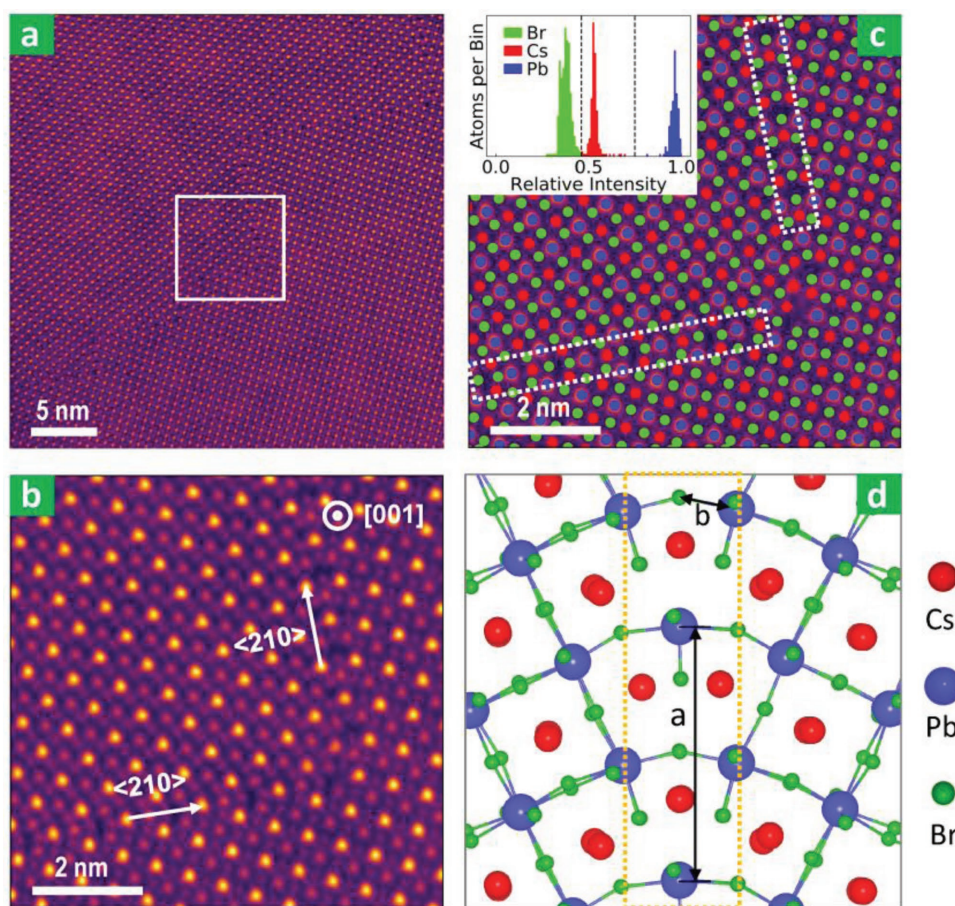
**ADVANCED
SCIENCE NEWS**
www.advancedsciencenews.com

**ADVANCED
MATERIALS**
www.advmat.de

Figure 2. a) HAADF image of a symmetrical GB, Br-rich [001](210) Σ5, found in CsPbBr$_3$ nanocrystals. b) Atomic-resolution HAADF image of a selected region as indicated by a white square in (a). c) Atomic assignment of the structure in (b) according to the Z-contrast intensity of individual atomic columns, and d) the corresponding structure optimized using DFT computations. The distances a and b in (d) are 13.27 and 3.04 Å, respectively.

the in-plane distance between two neighboring Pb atoms that are shared by both grains is 13.27 Å (marked as a in Figure 2d) and the in-plane Pb−Br bond distance related to the shared Br atom (marked as b in Figure 2d) is 3.04 Å, both of which match well with the respective distances of 13.16 and 3.08 Å in the experimental image. The GB angle of 128.0° obtained from DFT also agrees well with the experimental angle of 127.3°. The simulated STEM image of the structure in Figure 2d and its comparison with experimental image can be found in Section S3 in the Supporting Information. According to the coincidence-site-lattice model, we assign this GB as [001](210)Σ5, where [001] denotes the out-of-plane crystalline direction and (210) denotes the plane parallel to the GB. The HAADF images and analyses of a less common asymmetrical Σ17 GB and several other types of GBs can be found in Section S2 in the Supporting Information.

The structure of Σ5 GB discovered in this work is different from the previously known Σ5 GBs, both those derived from oxide perovskites and those proposed theoretically for lead-halide perovskites. For instance, the Br-rich GB found in this work (**Figure 3**a) is different from the [001](210)Σ5 GB found in SrTiO$_3$[21] (Figure 3b) and the proposed most stable theoretical GB in CsPbX_3[16] (Figure 3c), in terms of their Cs/Br

stoichiometry. Figure 3a is also significantly different from the [001](310)Σ5 GB reported in oxide perovskites[22] (Figure 3d) and that reported in CH$_3$NH$_3$PbI$_3$[23] and CsPbBr$_3$[16] (Figure 3e). Our thermodynamic calculations under Br- and Cs-rich conditions show that the relative energy of GBs in Figure 3a–e is 0.1, 0.0, 3.9, 6.0, and 0.8 eV per shared Pb atom, respectively, which indicates that the structure in Figure 3b would also be observed when the growth is close to thermal equilibrium, but the structures in Figure 3c–e are energetically unfavorable. This comparison demonstrates the necessity of combining STEM imaging and DFT calculations in resolving the GB structures of CsPbBr$_3$ under experimental conditions, which may not be necessarily under equilibrium.

Another typical type of planar defects found in the fused nanocrystals are RP planar faults, which consist of two CsBr layers with rock-salt stacking sandwiched between two CsPbBr$_3$ domains on either side. **Figure 4**a shows that the RP planar fault can propagate along the (010) and (100) planes throughout the nanocrystals and form a 90° step at each intersection. An atomic resolution HAADF image of the RP planar fault is shown in Figure 4b and the Z-contrast atomic assignment in Figure 4c clearly shows the rock-salt stacking of CsBr bilayers. Our DFT-optimized atomic structure of the RP planar fault is
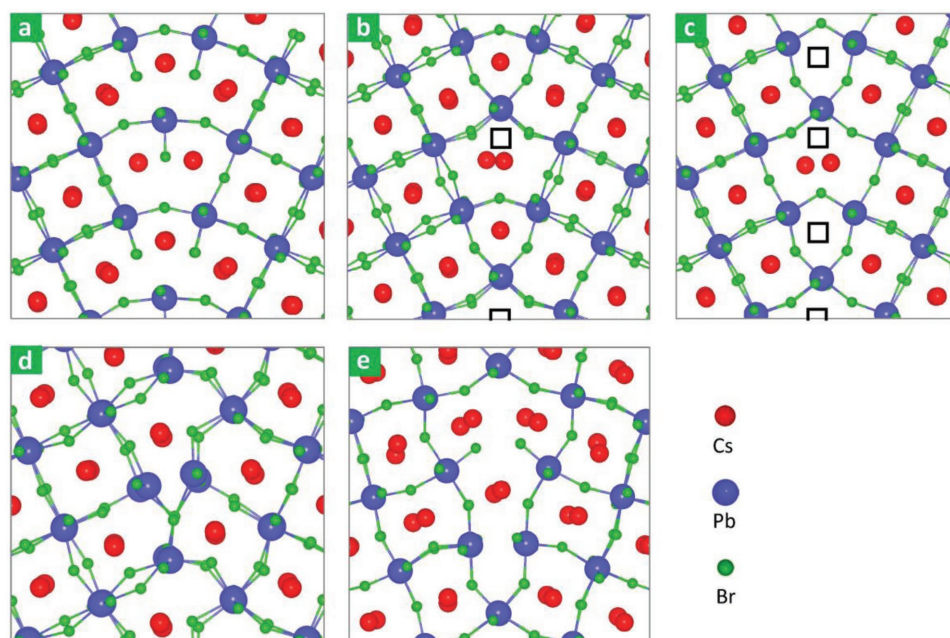
Figure 3. Comparison of various $\Sigma 5$ GBs in CsPbBr$_3$: a) [001](210)$\Sigma 5$ GB discovered in this work, b) [001](210)$\Sigma 5$ GB based on structures reported in ref. [21], c) [001](210)$\Sigma 5$ GB based on structures reported in ref. [16], d) [001](210)$\Sigma 5$ GB based on structures reported in ref. [21], and e) [001](310)$\Sigma 5$ GB based on structures reported in refs. [16,22,23]. The blank squares in (b) and (c) correspond to vacancies relative to the structure in (a).

shown in Figure 4d. We find that the average layer distance between the CsBr bilayer is predicted to be 3.70 Å by DFT, which is in good agreement with the experimental value of 3.59 Å based on analysis of the HAADF image in Figure 4c. The rumpling of Br atoms in Figure 4d is difficult to quantify from the HAADF image because the Z-contrast of Br atoms is too weak relative to the heavier cations, as confirmed by our simulated STEM image of Figure 4d and its comparison with the experimental image (see Section S3, Supporting Information). Besides the noticeable RP planar faults observed in the (100) and (010) planes, we also notice the evidence of its formation in the (001) plane, similar to a previous observation in CsPbBr$_3$ nanosheets,[8] and a detailed analyses can be found in Section S4 in the Supporting Information.

In traditional semiconductors, planar defects often hinder charge transport and promote nonradiative recombination by inducing deep defect levels and/or charge barriers. Having obtained accurate atomic structures of GBs and RP planar faults in CsPbBr$_3$, we now investigate their impact on the electronic properties. Our DFT calculations indicate that neither the [001](210)$\Sigma 5$ GB nor the RP planar fault introduces any defect levels in the bandgap, as shown in the density of states (DOS) plots in **Figure 5**a. Since planar defects could serve as a sink for point defects and thus exhibit dynamic composition,[24–26] we have examined several additional structures by introducing Cs and/or Br vacancies to the experimentally confirmed $\Sigma 5$ GB and RP planar fault. One example for the $\Sigma 5$ GB is shown in Figure 5b and a complete list can be found in Section S5 in the Supporting Information. Interestingly, we find that most structures still do not show any defect states in the bandgap, except those involving Pb dangling bonds and/or Pb–Pb bonds, a phenomenon similar to that reported for point defects in CsPbBr$_3$.[27,28] For instance, Br vacancies in the structure

of Figure 5b result in the formation of Pb–Pb bonds, which induce a deep defect level within the bandgap (Figure 5a) and localized electron density around the Pb–Pb bonds (Figure 5b). These findings suggest that growth of CsPbX_3 under halogen-poor conditions should be avoided to minimize the deep defect levels induced by Pb dandling bonds or Pb–Pb bonds at GBs. We also examine the intersections formed by the [001](210) $\Sigma 5$ GBs and RP planar defects (see kinks in Figures 2 and 4) and find that these intersections do not introduce deep defect levels in the bandgap, same as their straight counterparts (see Section S6, Supporting Information).

We have further examined the band diagram across the [001](210)$\Sigma 5$ GB and the RP planar fault to understand their effect on electron and hole transport. The band diagrams are obtained through a layer-by-layer projection of the density of states (LDOS) and are shown in **Figure 6**a,b for the GB and the RP fault, respectively. We find that the $\Sigma 5$ GB results in a relatively small band bending whereas the RP planar fault leads to a large band offset. Specifically, the conduction band offset ΔE_{CBM} and the valence band offset ΔE_{VBM} is 86 and 37 meV for the $\Sigma 5$ GB, and 134 and −193 meV for the RP planar fault, respectively. Therefore, around room temperature (with a thermal energy of ≈26 meV), the $\Sigma 5$ GB repels electrons and partially attracts holes like that of an n–p–n junction, while the RP planar fault repels both electrons and holes like a semiconductor–insulator–semiconductor junction. The band offsets are consistent with the charge density of the VBM and CBM at the $\Sigma 5$ GB and RP planar fault. As shown in Figure 6c,d, the positive ΔE_{CBM} drives electrons away from both the $\Sigma 5$ GB and the RP planar fault, while the positive ΔE_{VBM} of $\Sigma 5$ GB attracts holes to it and the negative ΔE_{VBM} of RP planar fault repels holes away from it. The sharp change of ΔE_{CBM} versus smooth change of ΔE_{VBM} in RP planar fault (Figure 6b) is also clearly observed in Figure 6d.

**ADVANCED
SCIENCE NEWS**
www.advancedsciencenews.com
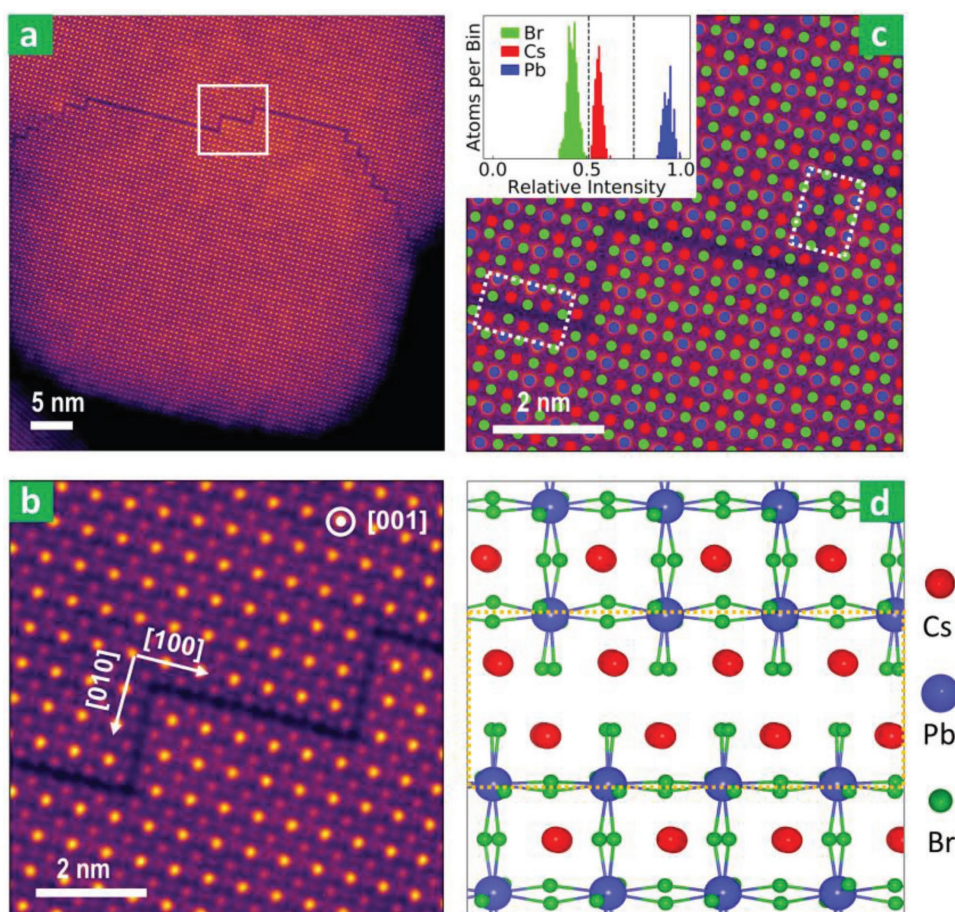
**ADVANCED
MATERIALS**
www.advmat.de

Figure 4. a) Low-resolution HAADF image of RP planar faults propagating through two fused nanocrystals. b) Atomic-resolution HAADF image of a selected region indicated by the white square in (a). c) Atomic assignment of the structure in (b) according to Z-contrast intensities. d) Atomic model of the RP planar fault optimized using DFT.

These band offsets can be qualitatively understood according to the composition of the planar defects and the band structure of $CsPbBr_3$. As shown in Figures 5,6c,d, and previous literature,[28] the VBM of bulk $CsPbBr_3$ consists of antibonding states from 6s electrons of Pb and 4p electrons of Br, and the CBM consists of the antibonding states from the 6p electrons of Pb and 4p electrons of Br. Because the [001](210)Σ5 GB has a composition of $CsPbBr_{3+\delta}$, such Br-rich environment is expected to increase the antibonding interaction between Pb and Br, which increases the bandgap and induces the positive ΔE_{VBM} and ΔE_{CBM} in Figure 6a. Because the RP planar fault has a significantly different stoichiometry (CsBr) relative to $CsPbBr_3$, a similar perturbation-based understanding as of the Σ5 GB is invalid. However, we find that the band diagram of RP planar fault is closely related to that of $CsPbBr_3$/CsBr heterojunction, where the bulk CsBr induces a negative ΔE_{VBM} and positive ΔE_{CBM} relative to $CsPbBr_3$ (see Section S7, Supporting Information).

Several implications can be anticipated based on the electronic properties of the [001](210)Σ5 GB and RP planar fault. Since the Σ5 GB partially repels electrons but conducts holes relatively well, it could be engineered to reduce the thermal conductivity by increasing phonon scattering while retaining bulk-like hole conductivity, which may find application as p-type electrode in thermoelectric devices. Additionally, the Σ5 GB could help separate the electron–hole pairs in solar cells, similar to the GBs of CdTe solar cells.[29] For the RP planar fault, since it serves as an effective electron and hole barrier and naturally binds two $CsPbBr_3$ regions with a sharp interface, it could be utilized to impose strong quantum confinement in large nanocrystals.[18] Since both Σ5 GBs and RP planar defects exhibit noticeable upward bending for CBM, both the planar defects should be minimized for use of $CsPbBr_3$ in light-emitting devices, which typically favor the type-I band diagram with downward bending for CBM and upward bending for VBM.

In view of the structural similarities, our findings on $CsPbBr_3$ could help explain previous intriguing and diverging results about the role of GBs in organic–inorganic lead-halide perovskites. On one hand, local fluorescence lifetime imaging experiments have shown that the GBs of $CH_3NH_3PbI_3$ show lower photoluminescence (PL) intensity relative to the center of the grains.[13,14] On the other hand, previous experiments based on Kelvin probe force microscopy and conductive atomic force microscopy found that GBs could benefit the charge separation and increase the photovoltage.[11] These seemingly conflicting results could be explained by the two aspects of
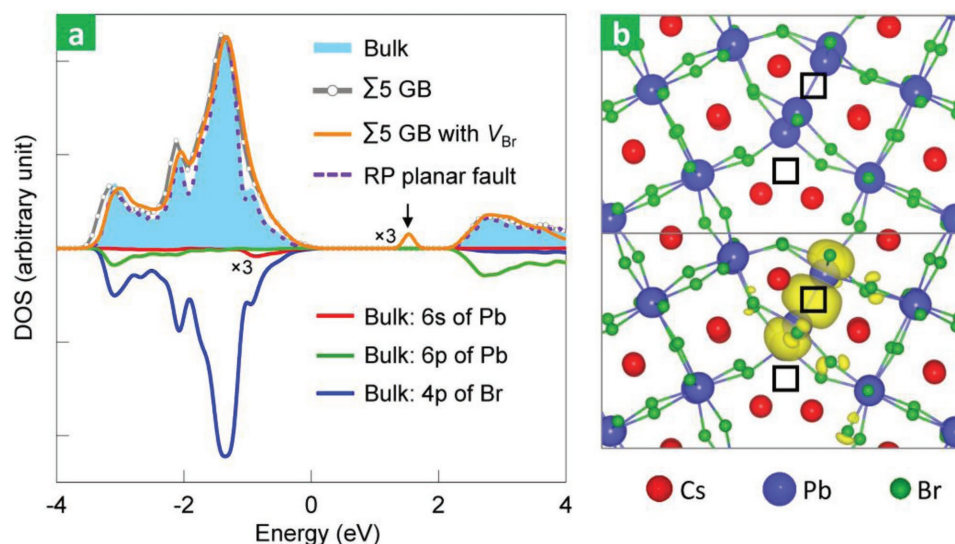
ADVANCED
SCIENCE NEWS
www.advancedsciencenews.com

ADVANCED
MATERIALS
www.advmat.de

Figure 5. a) Upper: comparison of DOS among bulk $CsPbBr_3$, the $\Sigma 5$ GB discovered in this work without and with V_{Br}, and the RP planar fault. The curves are magnified to match the highest peaks for easy comparison. Lower: orbital decomposition of the DOS of bulk $CsPbBr_3$. For easy visualization, the in-gap defect states of $\Sigma 5$ GB with V_{Br} and the curve corresponding to 6s of Pb have been magnified by three times. b) Structure of $\Sigma 5$ GB with V_{Br} and electron density of its defect state indicated by arrow in (a). Blank squares in (b) correspond to vacancies relative to the Br-rich $\Sigma 5$ GB discovered in this work.
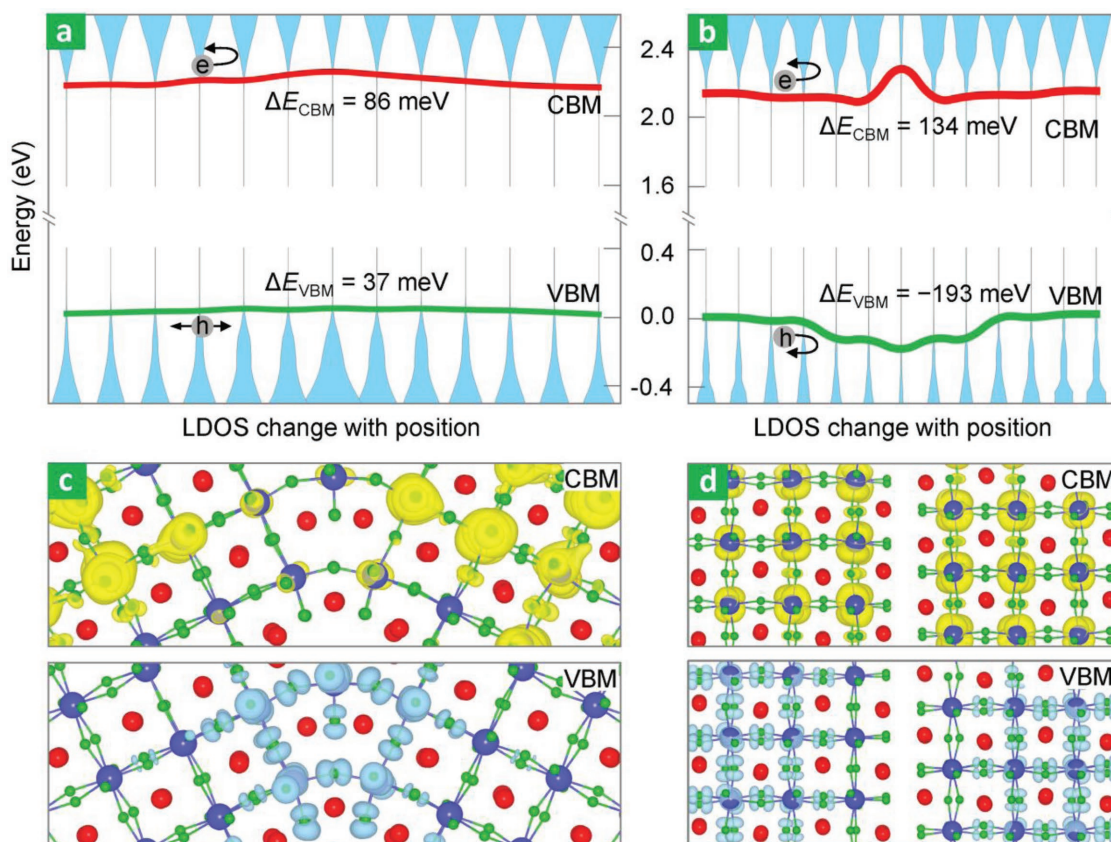

Figure 6. a,b) LDOS and band diagram of the $\Sigma 5$ GB (a) and the RP planar fault (b). c,d) Charge density of CBM and VBM for the $\Sigma 5$ GB (c) and the RP planar fault (d). For LDOS analyses, two neighboring atomic layers are chosen to contain the same integer number of $CsPbBr_3$ formula units, except at the planar defect. For band offset analyses, the band edge is picked as a LDOS constant to produce the bandgap in the internal region.

1805047 (6 of 8)

**ADVANCED
SCIENCE NEWS**

www.advancedsciencenews.com

**ADVANCED
MATERIALS**

www.advmat.de

GBs: defect levels and band offsets. As we have shown, the Br-rich [001](210)Σ5 GB does not exhibit deep defect levels but the Br-deficient ones do, which explains the low PL intensity at the GBs and significant improvement after halogen treatment.[7,14] Since the halide-rich [001](210)Σ5 GB repels electrons but attracts holes, it could indeed help separate the excitons and increase the photovoltage.

In summary, we have combined nanocrystal synthesis, STEM characterization, and DFT calculations to systematically investigate two commonly observed planar defects in CsPbBr$_3$ nanocrystals: GBs and RP planar faults. We have revealed the structure of these two planar defects with atomic precision and showed that the GBs observed in the lead-halide perovskites are different from those in oxide perovskites. We find that both types of planar defects do not show deep defect levels as long as there are no Pb dangling bonds or Pb—Pb bonds, but they produce band offsets that are significant enough to impact the charge transport and electron–hole recombination. Our results thus disprove an assumption that since CsPbBr$_3$ are tolerant to many point defects, its planar defects would also have negligible impact on its electronic properties. Overall, by elucidating the atomic and electronic structure of the GBs and RP planar faults under real growth conditions, our findings provide a path to controlling and even engineering these faults to achieve the full potential of CsPbBr$_3$ in particular, and lead-halide perovskites in general.

Experimental Section

Nanocrystal Growth: CsPbBr$_3$ nanocrystals were synthesized using a hot-injection technique, as described by Protesescu et al.[2] Diethylzinc was then used to fuse these as-synthesized nanocrystals to form larger nanocrystals. 0.2 M diethylzinc in anhydrous *n*-heptane solution was injected to the as-synthesized CsPbBr$_3$ nanocrystals in a glovebox under Ar atmosphere at room temperature. It is found that 5 wt% of diethylzinc led to enhanced fusion growth of the nanocrystals with relatively uniform size distribution. After the injection of diethylzinc, the nanocrystal colloid solution was stirred for 1 min in the glovebox and was subsequently diluted with anhydrous *n*-heptane in 1:10 volume ratio in ambient air. More details could be found in the previous work focusing on fusion growth of these nanocrystals.[18]

STEM Characterization: The STEM experiments were carried out using the aberration-corrected (equipped with fifth-order aberration corrector) Nion UltraSTEM 200 (operated at 200 kV) and Nion UltraSTEM 100 (operated at 100 kV) at Oak Ridge National Laboratory. Gaussian blurring was used to smooth out the HAADF images to accurately determine the position of the respective atomic columns. The nanocrystals were deposited on a carbon support TEM grid by drop casting. The grids were heated to 160 °C in vacuum to remove surface impurities prior to STEM experiments. The in-plane lattice constants for the HAADF image were calibrated to 8.49 and 8.15 Å, which were the refined lattice constants of CsPbBr$_3$ nanocrystals with an edge length of 12.5 nm obtained from ref. [30].

Computational Details: The first-principles modeling was based on DFT, as implemented in the Vienna *Ab initio* Simulation Package.[31] The Perdew–Burke–Ernzerhof[32] exchange-correlation functional was used. The plane-wave energy cutoff was set to 400 eV and the projector augmented wave method[33] was utilized with the following potentials: Cs_sv_GW($5s^25p^66s^1$) for Cs, Pb_d_GW($5s^25d^{10}6s^26p^2$) for Pb, and Br_GW($4s^24p^5$) for Br. The orthorhombic structure of CsPbBr$_3$ as confirmed for its nanocrystals was adopted.[30] The supercell size of the Σ5 GBs was about $11.8 \times 13.3 \times 75.9$ Å^3 and the RP planar fault was $8.2 \times 8.5 \times 90.2$ Å^3. The Brillouin zone was sampled using

Monkhorst–Pack *k*-points grid of $3 \times 3 \times 1$ and $4 \times 4 \times 1$ for the GB and the RP fault, respectively. Two or three atomic layers parallel to the planar defect were fixed to their bulk positions to simulate the internal region of grains, while the remaining atoms were relaxed till the force on each atom is less than 0.01 eV Å^{-1}. The optimized structures mentioned in the main text and Supporting Information can be found in the Supporting Data Set.

Supporting Information

Supporting Information is available from the Wiley Online Library or from the author.

Conflict of Interest

The authors declare no conflict of interest.

[1] C. C. Stoumpos, M. G. Kanatzidis, *Adv. Mater.* **2016**, *28*, 5778.

[2] L. Protesescu, S. Yakunin, M. I. Bodnarchuk, F. Krieg, R. Caputo, C. H. Hendon, R. X. Yang, A. Walsh, M. V. Kovalenko, *Nano Lett.* **2015**, *15*, 3692.

[3] Q. A. Akkerman, V. D'Innocenzo, S. Accornero, A. Scarpellini, A. Petrozza, M. Prato, L. Manna, *J. Am. Chem. Soc.* **2015**, *137*, 10276.

[4] W. J. Yin, T. Shi, Y. Yan, *Adv. Mater.* **2014**, *26*, 4653.

[5] W.-J. Yin, T. Shi, Y. Yan, *Appl. Phys. Lett.* **2014**, *104*, 063903.

[6] a) A. Buin, R. Comin, J. Xu, A. H. Ip, E. H. Sargent, *Chem. Mater.* **2015**, *27*, 4405; b) J. Kang, L. W. Wang, *J. Phys. Chem. Lett.* **2017**, *8*, 489.

[7] W. S. Yang, B. W. Park, E. H. Jung, N. J. Jeon, Y. C. Kim, D. U. Lee, S. S. Shin, J. Seo, E. K. Kim, J. H. Noh, S. I. Seok, *Science* **2017**, *356*, 1376.

[8] Y. Yu, D. Zhang, P. Yang, *Nano Lett.* **2017**, *17*, 5489.

[9] L. Gomez, C. Lin, C. de Weerd, L. Poirier, S. C. Boehme, E. von Hauff, Y. Fujiwara, K. Suenaga, T. Gregorkiewicz, *ACS Appl. Mater. Interfaces* **2018**, *10*, 5984.

ADVANCED
SCIENCE NEWS
www.advancedsciencenews.com

ADVANCED
MATERIALS
www.advmat.de

[10] E. Edri, S. Kirmayer, S. Mukhopadhyay, K. Gartsman, G. Hodes, D. Cahen, *Nat. Commun.* **2014**, *5*, 3461.

[11] J. S. Yun, A. Ho-Baillie, S. Huang, S. H. Woo, Y. Heo, J. Seidel, F. Huang, Y.-B. Cheng, M. A. Green, *J. Phys. Chem. Lett.* **2015**, *6*, 875.

[12] J. Xu, A. Buin, A. H. Ip, W. Li, O. Voznyy, R. Comin, M. Yuan, S. Jeon, Z. Ning, J. J. McDowell, P. Kanjanaboos, J. P. Sun, X. Lan, L. N. Quan, D. H. Kim, I. G. Hill, P. Maksymovych, E. H. Sargent, *Nat. Commun.* **2015**, *6*, 7081.

[13] N. De Marco, H. Zhou, Q. Chen, P. Sun, Z. Liu, L. Meng, E. P. Yao, Y. Liu, A. Schiffer, Y. Yang, *Nano Lett.* **2016**, *16*, 1009.

[14] D. W. deQuilettes, S. M. Vorpahl, S. D. Stranks, H. Nagaoka, G. E. Eperon, M. E. Ziffer, H. J. Snaith, D. S. Ginger, *Science* **2015**, *348*, 683.

[15] a) M. Kim, G. Duscher, N. D. Browning, K. Sohlberg, S. T. Pantelides, S. J. Pennycook, *Phys. Rev. Lett.* **2001**, *86*, 4056; b) T. Mizoguchi, Y. Sato, J. P. Buban, K. Matsunaga, T. Yamamoto, Y. Ikuhara, *Appl. Phys. Lett.* **2005**, *87*, 241920.

[16] Y. Guo, Q. Wang, W. A. Saidi, *J. Phys. Chem. C* **2017**, *121*, 1715.

[17] M. Kulbak, D. Cahen, G. Hodes, *J. Phys. Chem. Lett.* **2015**, *6*, 2452.

[18] M. V. Morrell, X. He, G. Luo, A. S. Thind, T. A. White, J. A. Hachtel, A. Y. Borisevich, J.-C. Idrobo, R. Mishra, Y. Xing, *ACS Appl. Nano Mater.* **2018**, *1*, 6091.

[19] S. J. Pennycook, D. Jesson, *Ultramicroscopy* **1991**, *37*, 14.

[20] a) S. Wei, Y. C. Yang, X. J. Kang, L. Wang, L. J. Huang, D. C. Pan, *Chem. Commun.* **2016**, *52*, 7265; b) S. ten Brinck, I. Infante, *ACS Energy Lett.* **2016**, *1*, 1266.

[21] M. Kim, G. Duscher, N. D. Browning, K. Sohlberg, S. T. Pantelides, S. J. Pennycook, *Phys. Rev. Lett.* **2001**, *86*, 4056.

[22] M. Imaeda, T. Mizoguchi, Y. Sato, H. S. Lee, S. D. Findlay, N. Shibata, T. Yamamoto, Y. Ikuhara, *Phys. Rev. B* **2008**, *78*, 245320.

[23] W. J. Yin, T. Shi, Y. Yan, *Adv. Mater.* **2014**, *26*, 4653.

[24] J. H. Jang, Y. M. Kim, Q. He, R. Mishra, L. Qiao, M. D. Biegalski, A. R. Lupini, S. T. Pantelides, S. J. Pennycook, S. V. Kalinin, A. Y. Borisevich, *ACS Nano* **2017**, *11*, 6942.

[25] J. Gazquez, R. Guzman, R. Mishra, E. Bartolome, J. Salafranca, C. Magen, M. Varela, M. Coll, A. Palau, S. M. Valvidares, P. Gargiani, E. Pellegrin, J. Herrero-Martin, S. J. Pennycook, S. T. Pantelides, T. Puig, X. Obradors, *Adv. Sci.* **2016**, *3*, 1500295.

[26] M. A. Frechero, M. Rocci, G. Sanchez-Santolino, A. Kumar, J. Salafranca, R. Schmidt, M. R. Diaz-Guillen, O. J. Dura, A. Rivera-Calzada, R. Mishra, S. Jesse, S. T. Pantelides, S. V. Kalinin, M. Varela, S. J. Pennycook, J. Santamaria, C. Leon, *Sci. Rep.* **2015**, *5*, 17229.

[27] H. Shi, M.-H. Du, *Phys. Rev. B* **2014**, *90*, 174103.

[28] J. Kang, L. W. Wang, *J. Phys. Chem. Lett.* **2017**, *8*, 489.

[29] C. Li, Y. L. Wu, J. Poplawsky, T. J. Pennycook, N. Paudel, W. J. Yin, S. J. Haigh, M. P. Oxley, A. R. Lupini, M. Al-Jassim, S. J. Pennycook, Y. F. Yan, *Phys. Rev. Lett.* **2014**, *112*.

[30] P. Cottingham, R. L. Brutchey, *Chem. Commun.* **2016**, *52*, 5246.

[31] G. Kresse, J. Furthmuller, *Phys. Rev. B* **1996**, *54*, 11169.

[32] J. P. Perdew, K. Burke, M. Ernzerhof, *Phys. Rev. Lett.* **1996**, *77*, 3865.

[33] P. E. Blöchl, *Phys. Rev. B* **1994**, *50*, 17953.